PLOS Complex Systems

RESEARCH ARTICLE

Deciphering and steering population-level response under spatial drug heterogeneity on microhabitat structures

Zhijian Hu[1,2,3*], **Kevin Wood**[1,3,4†]

1 Department of Biophysics, University of Michigan, Ann Arbor, Michigan, United States of America, **2** Department of Mathematics, University of Michigan, Ann Arbor, Michigan, United States of America, **3** Center for the Study of Complex Systems, University of Michigan, Ann Arbor, Michigan, United States of America, **4** Department of Physics, University of Michigan, Ann Arbor, Michigan, United States of America

† Deceased
* zhijianh@umich.edu

OPEN ACCESS

Citation: Hu Z, Wood K (2026) Deciphering and steering population-level response under spatial drug heterogeneity on microhabitat structures. PLOS Complex Syst 3(6): e0000113. https://doi.org/10.1371/journal.pcsy.0000113

Editor: Daniel Burbano, Rutgers University: Rutgers The State University of New Jersey, UNITED STATES OF AMERICA

Received: July 18, 2025

Accepted: June 8, 2026

Published: June 30, 2026

Data availability statement: No experimental datasets were used or generated in this work. Python code used to produce the results included in this work can be found at the GitHub repository https://github.com/Zzzzzhijian/Collective_Response_SpatialHetero_Public.git.

Abstract

Bacteria and cancer cells inhabit spatially heterogeneous environments, where migration shapes microhabitat structures critical for colonization and metastasis. The interplay between growth, migration, and spatial structure complicates the prediction of population responses to drug treatment, such as clearance or persistence, even under the same spatially averaged growth rate. Accurately predicting these responses is essential for designing effective treatment strategies. Here, we propose a minimal growth-migration model to study population dynamics on discrete microhabitat structures under spatial drug heterogeneity. By applying a kernel transformation, we map the original structure to an effective fully connected graph and derive a new exact criterion for population response based on a regularized Laplacian kernel reweighted by local growth rates. This criterion connects to forest closeness centrality and yields analytical bounds and sufficient conditions for population growth or decline. We find that higher structural connectivity, such as increased migration, generally promotes decline. Our framework also informs optimal spatial drug assignments, which reduce to selecting interconnected subcores in the effective complete graph. For partially controllable microhabitats or unknown drug distributions, we identify strategies that ensure population decline. As a clinical illustration, applying the framework to a parameterised model of colorectal cancer metastasis under systemic chemotherapy identifies the lung as a critical growth reservoir whose poor drug penetration sustains the population even when the spatially averaged response would predict decline, suggesting lung-targeted delivery as a route to robust clearance. Overall, our results offer a new theoretical perspective on drug response in spatially structured populations and provide practical guidance for optimizing spatially explicit dosing strategies in heterogeneous environments.

Funding: This work was supported by the National Institutes of Health (R35GM124875 to K.W.). The funders had no role in study design, data collection and analysis, decision to publish, or preparation of the manuscript.

Competing interests: The authors have declared that no competing interests exist.

Author summary

Understanding how populations of cells - such as bacteria or cancer cells - respond to drug treatments is essential for improving medical outcomes. However, predicting these responses can be challenging because the environment in which cells grow is often complex and spatially varied. In this study, we developed a new mathematical approach that transforms complicated spatial structures into simpler networks, allowing us to precisely predict when cell populations will grow or decline under different spatial drug conditions. Our framework identifies key locations within the environment that most influence treatment outcomes and offers practical guidelines for determining optimal drug dosing strategies. These findings provide new insights that could improve treatments for infections and cancer by more effectively controlling how drugs are spatially distributed within tissues.

Introduction

Healthcare-related cell communities, such as bacterial infections and cancer, have increasingly been recognized as complex ecosystems over the past decades [1–3]. These systems exhibit emergent collective behaviors, including antibiotic resistance and cancer invasion, which arise from the interplay of ecological and evolutionary processes. The complex interactions between different phenotypes and genotypes have inspired novel therapeutic approaches, such as containment strategies and adaptive therapies [4–8], which leverage competition between cell types. From a dynamical systems perspective, drugs constitute an integral part of the environment, and their interactions with cells, particularly under spatially heterogeneous drug distributions, have gained attention in recent years [9–17].

This paper focuses on short-term, ecological-timescale population responses to drug treatment, distinct from evolutionary processes such as resistance acquisition. While at the evolutionary timescale spatial drug heterogeneity has been shown to modulate the evolution of drug resistance in both cancer [10,12,13] and bacterial systems [11,18], with theoretical work indicating that resistance can be either accelerated or decelerated depending on mutation and migration rates [15,17,19], an analogous variability appears at the much shorter ecological timescale of a single course of treatment, which is our focus here.

Even under identical drug dosages, patients exhibit different levels of pathogen or cancer cell clearance between the first treatment and the final day of therapy. For instance, despite a standard 14-day antibiotic treatment regimen, approximately 20% of patients fail to achieve sufficient clearance of H. pylori [20]. Similarly, cancer patients face recurrence risks due to insufficient clearance [5,21,22], which may be influenced by spatial heterogeneities in drug absorption and pharmacokinetics/pharmacodynamics (PK/PD) [14]. Unlike well-mixed laboratory conditions, the in vivo tumor and microbial environments exhibit spatial complexity, making traditional

well-mixed drug-dose response measurements insufficient for predicting clinical outcomes (Fig 1). Recent work [23] has modeled population-level responses as an eigenvalue problem, where cell survival or extinction is governed by the interplay of spatial growth, migration, and microhabitat connectivity in a one-dimensional setting. This framework has been extended to model the emergence of multidrug resistance under natural selection [24]. However, the entanglement of structural, migratory, and growth-related factors in these eigenvalue formulations limits their interpretability. Additionally, clinical applications require extending these results beyond one-dimensional models to account for multiple discrete microhabitat scenarios such as cancer metastasis [25–30], lymph node networks [31–33], and bacterial translocation across body compartments [34–36].

To better understand how spatial drug heterogeneity shapes population-level responses (specifically, whether cell populations grow or decline), we develop a minimal growth-migration model defined on discrete microhabitat networks. In this model, local growth rates are constrained by drug-induced limits, ranging from a maximum drug-free growth rate to a minimum death rate. Migration allows for population movement across interconnected microhabitats, embedding spatial structure into the dynamics. We theoretically analyze this model by transforming the original network into an effective fully connected graph using a regularized Laplacian kernel. This transformation enables the derivation of an exact criterion for determining population response, reweighted by local growth rates and interpreted through a centrality measure known as forest closeness centrality. This centrality interpretation provides an efficient and analytically tractable condition for predicting whether a population will persist or be cleared under a given spatial drug distribution.

Interestingly, we find that increasing global structural diffusion, such as through enhanced migration or more inter-microhabitat connectivities, leads to a smooth transition from population growth to decline when the spatial drug heterogeneity is fixed. For a given microhabitat structure, population dynamics are not only governed by the spatially averaged growth rate and the migration rate, but the spatial arrangement of growth rates still plays a critical role. Our framework

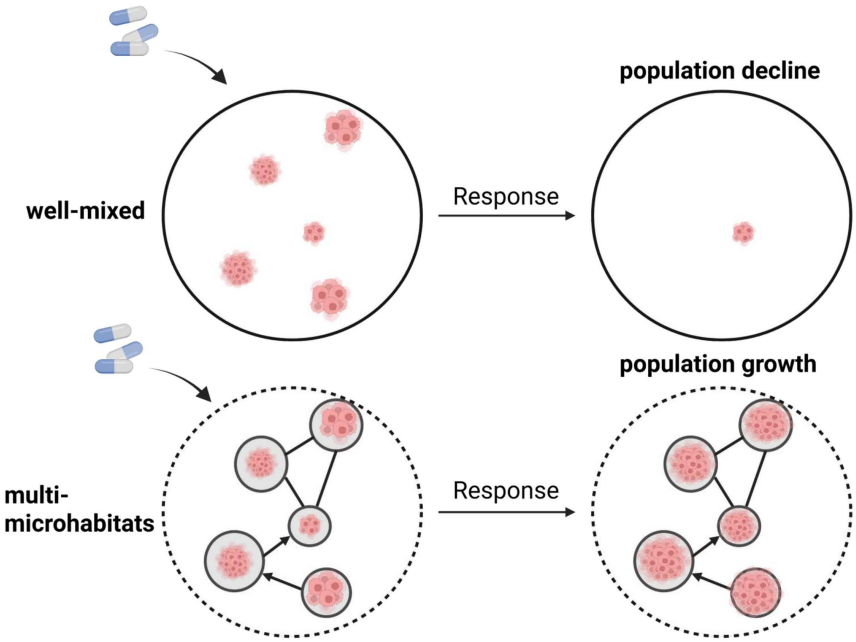

Fig 1. Contrasting population responses under spatial drug heterogeneity. Top: in a well-mixed environment, a spatially averaged growth rate $\langle g \rangle < 0$ is sufficient to predict population decline. Bottom: when cells inhabit a multi-microhabitat network with the same $\langle g \rangle < 0$, spatial drug heterogeneity can lead to population *growth* instead of decline, because sanctuary sites with poor drug penetration rescue the population. This contrast motivates the theoretical framework developed in this paper. Icons created with BioRender.com [48].

https://doi.org/10.1371/journal.pcsy.0000113.g001

informs optimal spatial drug assignments, which reduce to selecting interconnected subcores in the effective complete graph. For partially controllable microhabitats, we can design optimized strategies for population clearance; for unknown spatial drug heterogeneities, under a centrality-based heuristic, we identify parameters that ensure robust population decline, independent of spatial drug arrangements.

These findings have important implications for understanding and manipulating drug responses in complex biological systems. Health-related applications, such as bacterial infections and metastatic cancer, often involve heterogeneous spatial environments where growth, migration, and structure interact in nontrivial ways. Our framework offers a generalizable and analytically grounded approach to assess when populations will decline in such settings, providing a new lens through which to interpret treatment outcomes. Moreover, the model serves as a foundation for future extensions, including those incorporating temporal fluctuations, environmental feedback, or interspecies interactions. Clinically, this work highlights the potential of spatially explicit dosing strategies, tailored not only to drug strength but also to the structure of the tissue or infection site, to improve treatment outcomes for both infections and solid tumors.

Basic set-up of model system

Cell populations like bacteria or cancer cells can actively or passively move between different sites by migration or metastasis. Here we focus on passive, diffusion-like migration (e.g., hematogenous or lymphatic dissemination), in which the net flux between connected microhabitats is proportional to population density differences (see Discussion for the scope of this assumption). For the large population sizes typical of bacterial infections and clinically detectable cancers ($\sim 10^4 - 10^9$ cells), the dynamics are accurately captured by a deterministic, mean-field equation; the underlying stochastic master equation and its derivation as a large-population limit via the Van Kampen system-size expansion are presented in S1 File, Section S1. Letting $u = (u_1, u_2, \cdots, u_N)^T$ denote the vector of population densities across the N microhabitats, the resulting macroscopic growth-migration equation reads

$$\frac{du}{dt} = -\beta L u + G u = \Omega u \tag{1}$$

Here $\beta > 0$ is the migration rate (units: time^{-1}) governing the rate of passive dispersal between connected microhabitats, and L is the graph Laplacian matrix encoding the microhabitat connectivity structure: $L_{ij} = -1$ if microhabitats i and j are connected, and L_{ii} equals the degree of node i. $G = \mathrm{diag}(g_1, \ldots, g_N)$ is a diagonal matrix where each g_i is the net growth rate at microhabitat i under the local drug concentration. Equation (1) corresponds to linearized (exponential) growth, obtained from logistic growth by neglecting density-dependent competition; this approximation is appropriate for the short-term regime before populations approach carrying capacity, which is the focus of this work (see Limitations). Since drug-induced growth rates $\{g_i\}$ are bounded by physiology, we require $g_i \in [d_0, g_0]$, where $d_0 < 0$ is the maximum drug-saturated death rate and $g_0 > 0$ is the drug-free growth rate, both determined by cell type, drug type, and environmental factors such as nutrient availability [37–39]. For example, a Hill dose-response function maps the local drug concentration to $g_i \in [d_0, g_0]$, with $g_i \approx g_0$ at zero drug and $g_i \approx d_0$ at saturating drug concentration; this functional form is well-established for bactericidal antibiotics [40] and cytotoxic chemotherapy agents alike. Equation (1) is the minimal growth-migration model required to understand the short-term population response, defined here as the initial exponential phase of growth or decline before density dependence or resistance evolution becomes relevant (typically days to weeks in bacterial and cancer contexts [23]), under different spatial drug heterogeneities and microhabitat structures.

Since the drug concentration must be sufficiently high to eliminate cancer or bacterial cells, we require that the spatially averaged growth rate satisfies $\langle g \rangle = \frac{\sum_{i=1}^{N} g_i}{N} < 0$. For population decline or clearance, the condition $\Omega = G - \beta L \prec 0$ must hold, or equivalently, the largest eigenvalue $\lambda_0 = \|\Omega\| = \|G - \beta L\| < 0$. However, solving this exactly is typically intractable. Applying first-order perturbation theory, as in recent studies [23,24], we approximate the largest eigenvalue as

$$\lambda_0 \approx \langle g \rangle + \langle u_0 | \, \delta g \, | u_0 \rangle = \langle g \rangle$$

Since $u_0 = \frac{1}{\sqrt{N}}(1, 1, \ldots, 1)^T$, we obtain $\langle u_0 | \, \delta g \, | u_0 \rangle = 0$; note that u_0 assigns equal weight to every microhabitat, so the first-order correction vanishes identically regardless of the spatial arrangement of $\{g_i\}$. This means this approximation only captures well-mixed effects while neglecting spatial drug distribution and multi-microhabitat structure. Higher-order perturbation terms can in principle be computed analytically (see Discussion and S1 File, Section S1), but the resulting expressions grow rapidly in complexity and depend on the full eigenbasis of L, limiting their practical interpretability. This motivates the exact kernel transformation approach developed below.

Results

Kernel transformation and new criterion for population response

Instead of relying on perturbation theory, we derive an exact solution for the clearance or decline criterion based on a "kernel" transformation. For the kernel transformation, we first decompose G as $G = -|d_0| I + \sqrt{|d_0|} D^{\frac{1}{2}} \cdot \sqrt{|d_0|} D^{\frac{1}{2}}$, where I is the identity matrix and $D^{\frac{1}{2}} = \mathrm{diag}(\sqrt{\delta_1}, \ldots, \sqrt{\delta_N})$ is the diagonal positive-semidefinite square root of $D = \mathrm{diag}(\delta_1, \ldots, \delta_N)$, with the ith diagonal entry $\sqrt{\delta_i}$ where $\delta_i = 1 + \frac{g_i}{|d_0|} \in [0, c]$ encodes the relative growth information at microhabitat i compared to the maximum death rate $|d_0|$. Based on Schur complements (see S1 File, Section S2 for details), we show that the condition $\Omega = G - \beta L \prec 0$ is equivalent to

$$\lambda_{\max}(A) = \lambda_{\max}(D^{\frac{1}{2}} K D^{\frac{1}{2}}) < 1 \tag{2}$$

where $K = (I + \gamma L)^{-1}$ is the regularized Laplacian kernel matrix naturally emerging from our minimal growth-migration dynamics, and $\gamma = \frac{\beta}{|d_0|}$ is the ratio of the cell migration rate β to maximum drug-induced death rate $|d_0|$. Importantly, γ characterises the dispersal of the *cell population*, not the drug itself; drug concentrations are encoded in the $\{g_i\}$ and are assumed spatially fixed. γ effectively acts as a rescaled migration intensity, modulating how spatial structure shapes population outcomes.

The transformation $K = (I + \gamma L)^{-1}$ converts the original sparse microhabitat graph into an effective fully connected graph: every pair of microhabitats acquires a non-zero off-diagonal entry K_{ij}, whose magnitude reflects how strongly the two microhabitats are dynamically coupled through the network. This "kernel trick" is what allows us to work with a simpler, fully connected structure while retaining all information about the original sparse topology.

The matrix K, also known in some contexts as the *forest matrix* or the *parametrized matrix forest index*, has appeared in a wide range of network applications. It is at least row-stochastic (and becomes doubly stochastic for undirected graphs), mapping the original sparse structure into an effective, fully connected graph. Beyond our framework, the matrix K has been used in prior network-science applications: off-diagonal entries K_{ij} have quantified spatial proximity in disease-spread models [41] and for link prediction in biological networks [42–45]. Our work reveals a new role for K: its diagonal entries K_{ii} naturally emerge as the governing quantity for population-level growth-decline transitions under spatial drug heterogeneity. A particularly relevant measure derived from K is the *forest closeness centrality* [46,47], defined as

$$C_i = \frac{N}{K_{ii} + \mathrm{tr}(K) - 2} \propto K_{ii}^{-1}, \tag{3}$$

which approximately corresponds to the inverse of the diagonal element K_{ii}. For simplicity, we will refer to K_{ii}^{-1} as the centrality measure in this paper. While this matrix has traditionally been engineered for tasks such as node ranking, link prediction, or similarity assessment, our framework reveals its *natural appearance* as a kernel governing the interplay

between growth and migration. This connection provides a simple but novel interpretation of centrality as a predictor of population response and optimized clearance strategies, which we further illuminate in the subsequent sections.

Rewrite $\lambda_{\max}(A) = \lim_{k\to\infty} \left\|A^k\right\|^{1/k}$, where $\|\cdot\|$ is chosen as the infinite norm $|\cdot|_\infty$, the maximum row sum of absolute value of matrix A. A^k_{ij} here can be interpreted as the length-k walk from microhabitat i to microhabitat j. So now $\lambda_{\max}(A)$ becomes a special norm measuring the maximum total walk length from a microhabitat i to every microhabitat including i itself (see S1 File, Section S3 for details). Again, this tells us the new largest eigenvalue is capturing global information of the original multi-microhabitat structure. It's hard to find out the analytical solution of $\lambda_{\max}(A)$ due to the inhomgeneous nature of growth-weight distance between microhabitats. However, based on this walk-length interpretation, we find out the lower and upper bound for $\lambda_{\max}(A)$,

$$\max_i K_{ii}\,\delta_i \le \lambda_{\max}(A) \le \max_i \sum_j \sqrt{\delta_i\delta_j}\,K_{ij}, \tag{4}$$

where $K_{ii} \propto 1/C_i$ in the lower bound represents the inverse of forest closeness centrality, and the upper bound is the maximum row sum of length-1 walk (see S1 File, Section S3 for details). We can also treat each $\sqrt{\delta_i\delta_j}\,K_{ij}$ as the edge value of the efficient fully connected graph.Then these 2 bounds inform that, finding $\lambda_{\max}(A)$ here is approximately equivalent to identifying key microhabitats with maximum growth-weighted centrality, or with maximum weighted connectivities. $\lambda_{\max}(A) = \max_i K_{ii}\,\delta_i$ holds when microhabitat i becomes "effectively isolated," meaning $K_{ij} \approx 0$ for all $j \neq i$, so the node contributes negligibly to the walks in all other microhabitats; this occurs when a node has very few or very weak connections relative to the rest of the network (see S1 File, Section S4.3 for a formal criterion); $\lambda_{\max}(A) = \max_i \sum_j \sqrt{\delta_i\delta_j}$ holds when the structure has local symmetry and A becomes a circulant matrix (see S1 File, Section S4.1 for details). Either K_{ii} or K_{ij} contains global information of the original structure due to the kernel transformation. If we do the same calculation for $\Omega = G - \beta L$ instead of A, we can only find out $g_i - \beta k(i) \le \lambda_{\max}(\Omega) \le g_i$, where $k(i)$ is the degree of ith mcriohabitat. These are looser bounds only containing localized information like degree. So by doing the kernel formation, we can find out a tighter bound of $\lambda_{\max}$ with meaningful interpretations.

If $\max_i \sum_j \sqrt{\delta_i\delta_j}\,K_{ij} < 1$ or $\max_i K_{ii}\,\delta_i > 1$, we thus find out sufficient conditions for population decline or population growth (or $\max_i \sum_j \sqrt{\delta_i\delta_j}\,K_{ij} > 1$, $\max_i K_{ii}\,\delta_i < 1$ are necessary conditions for population growth, population decline). These 2 criteria can be applied to quickly determine population response without directly calculating $\lambda_{\max}(A)$ itself. While $\max_i \sum_j \sqrt{\delta_i\delta_j}\,K_{ij}$ is in a first-order form considering interaction effect, $\max_i K_{ii}\,\delta_i$ has zero-order form considering only centrality effect, decoupling growth information and structure information ($K_{ii} = \sum_{k=1}^{N} \frac{V_{ik}\left(V^{-1}\right)_{ki}}{1+\frac{\beta}{|d_0|}\omega_k}$, with V and $\{\omega_k\}$ representing the eigenvector matrix and eigenvalues of the Laplacian matrix L, respectively. It contains only structure information, with maximum drug-induced death rate $|d_0|$ as the baseline growth).

So in practice, we can always perform a quick diagnostic check of the population response using the quantity $\max_i K_{ii}\,\delta_i$. If $\max_i K_{ii}\,\delta_i > 1$, we can immediately predict population growth. Conversely, if $\max_i K_{ii}\,\delta_i < 1$, this provides a necessary condition for population decline. As a second step, we evaluate the upper bound $\max_i \sum_j \sqrt{\delta_i\delta_j}\,K_{ij}$; if this quantity is also smaller than 1, we can conclude that population decline will occur. Since the diagonal element K_{ii}, also known as the forest closeness centrality C_i, serves as a useful and interpretable indicator under growth-migration dynamics, we propose to refer to K_{ii} as the *inverse dynamic-related centrality*, and denote its reciprocal C_i as the *dynamic-related centrality*.

In this study, we primarily focus on how inverse centrality values K_{ii} can be leveraged to predict population responses. Because these responses are influenced by two spatial effects, namely spatial drug heterogeneity (i.e., the spatial growth distribution $\{\delta_i\}$) and the spatial structure of the system, we organize our analysis as follows:

- Given a fixed spatial drug heterogeneity $\{\delta_i\}$, we analyze how different microhabitat structures, as captured by the matrix K, influence population-level responses, and examine the role that K_{ii} plays in shaping these dynamics.

- Given a known multi-microhabitat structure (i.e., a fixed matrix K), we explore how different growth distributions $\{\delta_i\}$ affect the outcome, and how this insight can be used to optimize treatment strategies by exploiting structural information, particularly the inverse centralities K_{ii}.

Microhabitat structure effects under given spatial drug heterogeneity

We aim to investigate how microhabitat structures influence population responses under a fixed spatial drug heterogeneity. Specifically, we address the following questions: 1. How do different microhabitat structures with the same edge count (number of migration connections, i.e., the same total degree sum) affect population responses? 2. How does varying the level of connectivity (measured by edge density $\rho = |E|/\binom{N}{2}$) alter spatial drug responses across different structural configurations? Overall, our goal is to understand how structural effects on population dynamics can be predicted by the dynamic-related centrality C_i, or equivalently, by its inverse K_{ii}.

Distinct population responses induced by different multi-microhabitat structures predicted by kernel criteria. Starting from a fixed spatial drug heterogeneity (see Fig 2A), we demonstrate how different multi-microhabitat structures lead to distinct population responses, which can be precisely captured by checking $\max_i K_{ii}\,\delta_i$ and $\max_i \sum_j \sqrt{\delta_i \delta_j}\, K_{ij}$. The inverse value of dynamic-related centralities C are visualized for two different multi-microhabitat

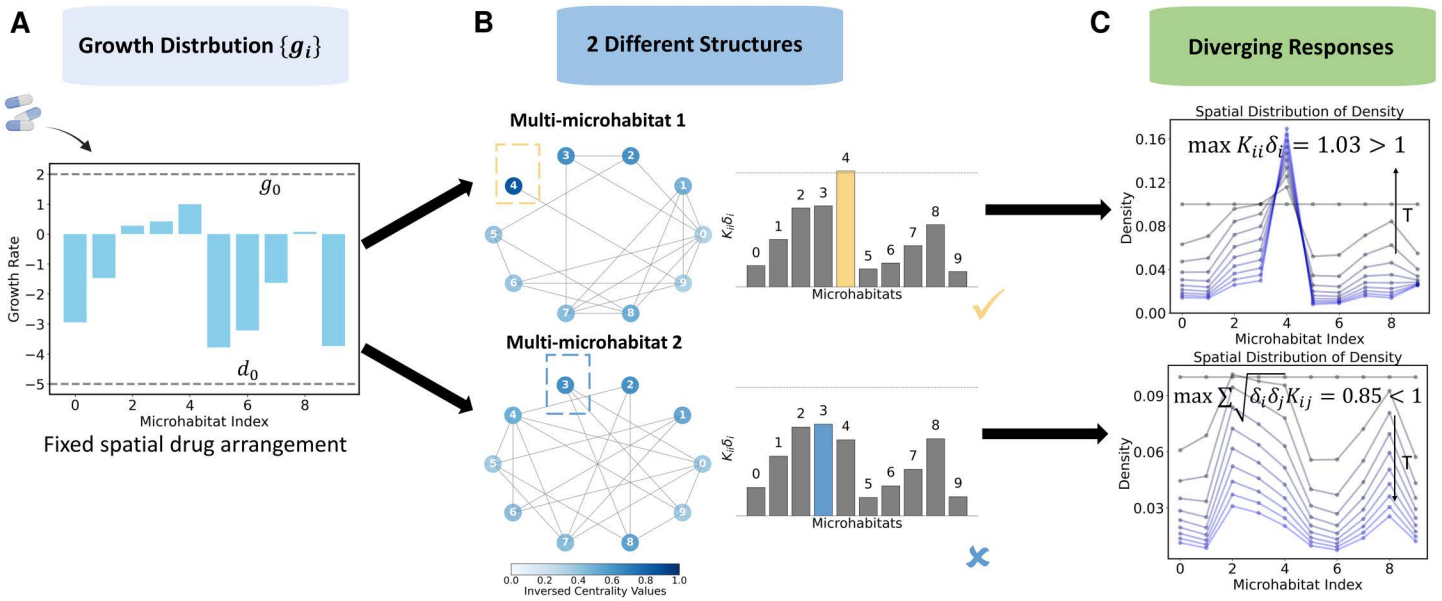

Fig 2. Different microhabitat structures with the same spatial growth distributions induce different population responses, explained by our criterion. A. Example distribution of spatial growth rates across 10 connected microhabitats. Growth rates are bounded by the drug-related maximum growth rate and death rate, represented by grey dashed lines. **B.** Two different microhabitat structures with the same number of microhabitats and migration connections, along with their corresponding $K_{ii}\delta_i$ values shown as bar plots. In each structure, colors indicate K_{ii}, the inverse of dynamic-related centrality values C_i, while different transparencies represent relative growth δ_i. The microhabitat with the highest $K_{ii}\delta_i$ in each structure is highlighted with a dashed rectangle, colored light yellow for population growth and light blue for population decline, as confirmed by the adjacent bar plots. Notably, the microhabitat with the highest K_{ii} does not necessarily correspond to the highest $K_{ii}\delta_i$. The yellow check mark near the top bar plot indicates that population growth is predicted by $\max_i K_{ii}\delta_i > 1$ (sufficient condition for growth; equivalently, necessary condition for decline). The light blue cross mark near the bottom bar plot indicates that $\max_i K_{ii}\delta_i < 1$ serves as a necessary condition for population decline, and further check of $\max_i \sum_j \sqrt{\delta_i\delta_j} K_{ij} < 1$ is required. **C.** Two spatial dynamic configurations demonstrating different population responses. The grey line represents the initial population density. As time increases, the density curves change from grey to dark blue. The dynamics induced by structure 1 exhibit a growth trend, consistent with our theoretical prediction, while those induced by structure 2 show a decline trend predicted by $\max_i \sum_j \sqrt{\delta_i\delta_j} K_{ij} < 1$. For both 2 structures, $\beta = 1$, $g_0 = 2$, $d_0 = -5$, $\langle g \rangle = -1.5$, and the edge number is fixed at $|E| = 10$. Icons created with BioRender.com [48].

https://doi.org/10.1371/journal.pcsy.0000113.g002

structures, with color gradients indicating different values (see Fig 2B). All values of inversed C (or K_{ii}) are upper bounded by 1 (see S1 File, Section S2). Different transparencies represent varying growth rate values.

Notably, the locations of $g_{\max}$ (or $\delta_{\max}$), $\max K_{ii}$, and $\max_i K_{ii}\,\delta_i$ do not necessarily coincide. We can approximate $K_{ii}\,\delta_i$ directly from the visualized networks by observing the color and transparency of microhabitats(nodes), which are highlighted in different colors. The adjacent bar plots reveal that in one structure, at least one $K_{ii}\,\delta_i$ value exceeds 1, whereas in the other, all values remain below 1. Consequently, the first multi-microhabitat structure leads to population growth, while the second indicatively results in decline. It's proved by checking $\max_i \sum_j \sqrt{\delta_i \delta_j}\, K_{ij} < 1$. The population decline is as illustrated by the spatial-temporal dynamics in Fig 2C. Our simple criterion thus serves as a computationally efficient predictive tool for population responses without requiring detailed dynamic simulations. Interestingly, the dynamic-related centrality $C_i = K_{ii}^{-1}$ is proportional to node degree and correlates with conventional centrality measures (see S1 File, Section S10), although the importance rankings may differ from those conventional measures. It bears strong similarity to closeness centrality. In the population responses of the 2 example structures we have shown, structure 2 with a lower coefficient of variation in node degree (more even connectivity) among different microhabitats, tend to decline compared to structure 1. This can be explained from a centrality perspective: high C usually represents good connectivities with other microhabitats, if under a relatively high-drug dose regime as shown in Fig 2A, the high C tends to connect with more "sink" microhabitats with negative growth rates, increasing the probability for population decline. In structure 1, the microhabitat 4, with positive growth rate and high inverse centrality value (low centrality C value), is effectively isolated, with only one connection to other microhabitats, thus increasing the chance of survival.

Increased connectivity accelerates centrality-predicted population decline. Since dynamic-related centrality reflects the importance of edge number, and the second structure with a more even connectivity in Fig 2 leads to population decline, it suggests that increasing global diffusion over different microhabitats can effectively decrease K_{ii}, thus mitigating population growth by $\max K_{ii}\delta_i < 1$. Increasing migration rate can be one way to enhance diffusion (from the spectral decomposition $K_{ii} = \sum_{k=1}^{N} \frac{V_{ik}\left(V^{-1}\right)_{ki}}{1+\gamma\omega_k}$, with V, $\{\omega_k\}$ the eigenvectors and eigenvalues of L: for a connected undirected graph the zero mode $\omega_1 = 0$ contributes $1/N$ regardless of β, so $K_{ii} \to 1/N$ as $\beta \to \infty$; more precisely, $K_{ii} - 1/N = O(\beta^{-1})$, i.e., the non-zero-mode correction decays as β^{-1}). Increasing the average number of edges or connection density may be another way to enhance global diffusion thus increasing the probability of population decline. To investigate this, we tune the edge density $\rho = \frac{|E|}{\binom{N}{2}}$, defined as the ratio of the total number of edges in a given graph to the number of edges in a complete graph, and examine its effect on $\max K_{ii}\delta_i$.

Using 1000 stochastic samples from random graph for each edge density, we observe that as edge density increases, sample-averaged $\max K_{ii}\delta_i$ decreases rapidly and eventually crosses the critical threshold $\max K_{ii}\delta_i = 1$ (see Fig 3). Fig 3A illustrates four different multi-microhabitat structures with increasing edge densities, where the colors gradually fade to white, indicating decreasing $\max K_{ii}\delta_i$ values. This finding suggests that densely connected microhabitats may require lower drug doses to induce population decline, whereas sparsely connected structures may necessitate higher drug doses to achieve the same effect.

Spatial drug heterogeneity effects and optimal strategy under a given multi-microhabitat structure

Different spatial drug heterogeneities, like different multi-microhabitat structures, induce distinct population responses. In our study, to allow meaningful comparison across scenarios, we control the spatially averaged drug dose - or equivalently, the spatially averaged growth rate $\langle g \rangle$ - in our minimal model. We consider two cases depending on whether spatial drug heterogeneity is controllable: 1. Fully controllable heterogeneity: Clinically, if we are fortunate enough to precisely control drug concentration at each microhabitat (or node), population decline can be achieved by selecting the spatial drug assignment that minimizes the largest eigenvalue - we simply find when $\min \lambda_{\max}(A) < 1$. This gives us the optimal spatial drug configuration among all possible combinations. 2. Uncontrollable or unknown heterogeneity: If spatial drug

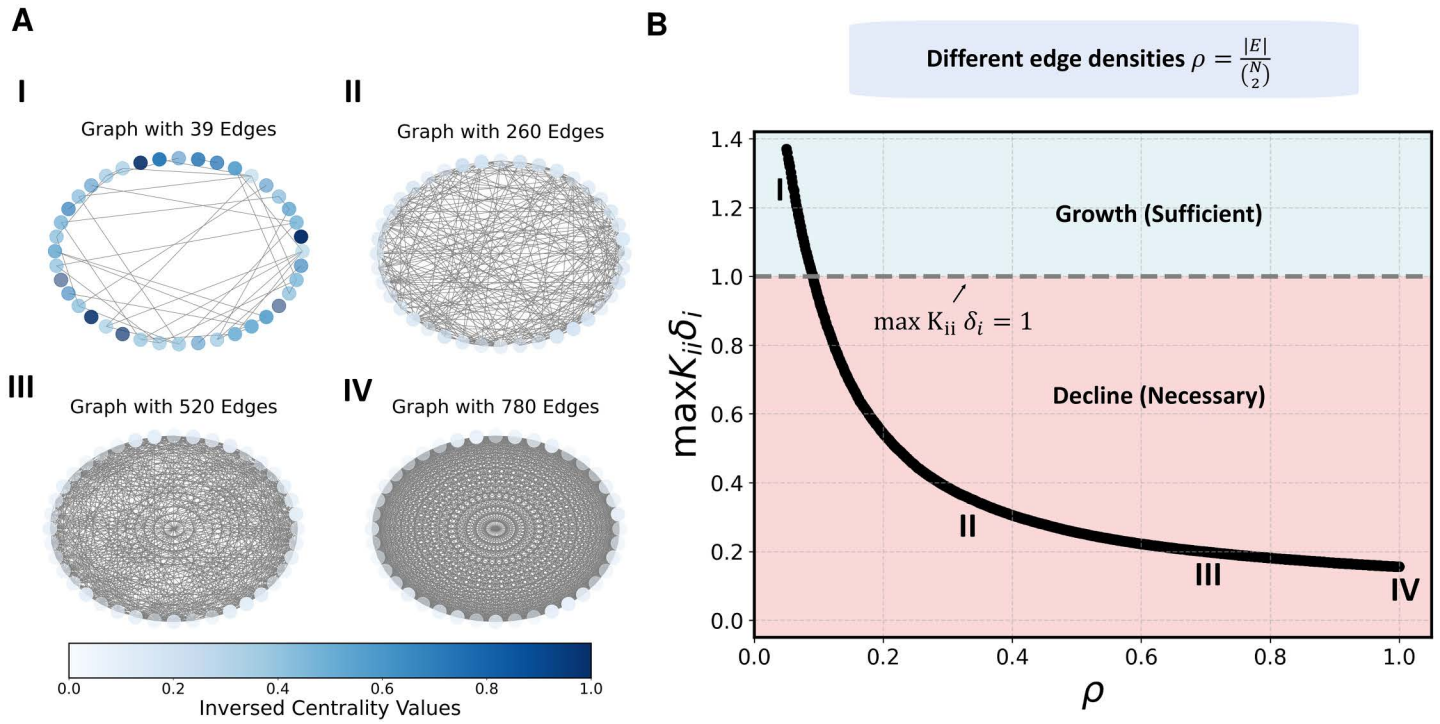

Fig 3. Increasing edge/connection density enhances the tendency for population decline. A. Four example microhabitat structures (microhabitat number $N = 40$) with varying connection densities but the same spatial growth rate distribution; structure IV is a fully connected (complete) graph. Color gradients represent dynamic-related centrality values C, while different transparencies indicate relative growth values δ. As connectivity increases, the colors gradually fade to white, indicating lower centrality values. **B.** The maximum $C\delta$ value decreases as connection density ρ increases. As the curve crosses the critical threshold $\max C\delta = 1$, population response shifts from growth to decline. Connectivity has a similar effect to migration rate (see S1 File, Section S5). The curve represents an average over 1000 stochastic samples of different random networks for each edge density. For parameters, $\beta = 0.5$, $g_0 = 2$, $d_0 = -1$, $\langle g \rangle = -0.25$.

https://doi.org/10.1371/journal.pcsy.0000113.g003

assignment cannot be precisely controlled or is unknown, we must ensure population decline under the worst-case spatial drug configuration. This requires $\max \lambda_{\max}(A) < 1$, ensuring a "robust" population decline, defined as $\lambda_{\max}(\Omega) < 0$ for *all* feasible drug distributions $\{g_i\} \subset [d_0, g_0]$ consistent with a given $\langle g \rangle$, that is independent of the specific drug distribution.

This naturally leads to a constrained optimization problem, as illustrated in recent work on robust decline under spatial drug heterogeneity in continuous 1D space [23]. In both cases, we are solving a constrained nonlinear optimization problem involving the largest eigenvalue. However, the search space is large, since each g_i varies continuously and the configuration space grows combinatorially with the number of microhabitats N.

Remarkably, the solution to this class of problems can be simplified. For the minimization case ($\min \lambda_{\max}(A)$), assuming $\langle g \rangle < 0$, the optimal strategy is always an interior point with every $0 < \delta_i < c$, or $d_0 < g_i < g_0$. This optimal strategy depends on K and is generally not analytically tractable. However, a uniform drug assignment $g_i = \langle g \rangle$ for all microhabitats (the "even-spread strategy") suffices to guarantee population decline under $\langle g \rangle < 0$. While achieving a perfectly uniform drug distribution in vivo is challenging (e.g., heterogeneous tumour vasculature), this result establishes a useful theoretical benchmark: any deviations from uniformity that worsen the outcome can be identified by comparing $\lambda_{\max}(A)$ under the actual distribution against this lower bound. For the maximization case ($\max \lambda_{\max}(A)$), the optimum typically lies on or near the active constraints (see S1 File, Section S6 for a detailed proof). This means that, for a fixed $\langle g \rangle$, we should assign as many microhabitats as possible to the maximum death rate d_0 or the maximum growth rate g_0, leaving at most one

remainder $g_r \in [d_0, g_0]$. The optimal configuration then takes the form $\{g_i\}_{\text{optimal}} = \{g_r; g_0, \cdots; d_0, \cdots\}$, which we refer to as the "one-remainder strategy." Hence, this continuous eigenvalue optimization problem reduces to a discrete combinatorial optimization. Interestingly, our kernel transformation is able to further simplify the problem. By expressing growth in terms of relative rates δ_i, the optimal growth configuration becomes $\{\delta_i\}_{\text{optimal}} = \{\delta_r; c, \cdots; 0, \cdots\}$, where $\delta_r \in [0, c]$, and $c = 1 + \frac{g_0}{|d_0|}$ is the maximum possible relative growth rate. For nodes assigned $g_i = d_0$, $\delta_i = 0$, which effectively removes all edges from microhabitat i to its neighbors under our transformation (as the structure becomes effectively fully connected). If $N - S$ microhabitats are suppressed ($\delta_i = 0$), the remaining effective graph forms an S-clique, and the matrix A reduces to a smaller principal submatrix A_S of size S. This matrix can be decomposed as:

$$\begin{aligned} A_S =& cK[S] \\ &+ (\Delta\sqrt{c})\left(e_1 k_1^\top + k_1 e_1^\top\right) \\ &+ \Delta^2 K_{11} e_1 e_1^\top \end{aligned} \tag{5}$$

Here, we assume the microhabitat with the remainder g_r is labeled 1; $c = 1 + \frac{g_0}{|d_0|}$, $\Delta = \sqrt{\delta_r} - \sqrt{c}$, $e_1 = (1, 0, \ldots, 0)^\top$, and $k_1 = \left(K_{11}, K_{21}, \ldots, K_{S1}\right)^\top$ is the first column of $K[S]$. K_{11} reflects the inverse dynamic-related centrality of the node with the remainder. Thus, solving the optimization problem becomes equivalent to selecting an S-clique from the full graph to minimize or maximize $\lambda_{\max}(A_S)$.

While discrete combinatorics optimization remains computationally challenging, we propose a centrality-based heuristic that leverages the decoupling of structure and growth. Under very high drug doses - i.e., when $d_0 \leq \langle g \rangle \leq \frac{N-1}{N} d_0 < 0$, or when $g_0 \geq (N-1)|d_0|$ - the one-remainder strategy becomes equivalent to selecting a single growing microhabitat. Then we have $\lambda_{\max}(A) = \delta_r K_{ii}$. To guarantee decline under unknown heterogeneity, we require $\max_i K_{ii} < \frac{1}{\delta_r}$, implying the structure must contain at least one relatively isolated microhabitat.

In the general case with multiple positive growth rates $\{\delta_r; c, \cdots\}$, we aim to identify an interconnected but relatively isolated S-clique to ensure robust decline. This intuition aligns with Fig 3B, where less connected graphs tend to suppress growth less effectively, thus serving as the "worst" case. Note that selecting the most isolated S-clique is not simply equivalent to minimizing the row sum of A_S, which is only an upper bound: $\lambda_{\max}(A_S) \leq \max_i \sum_j \sqrt{\delta_i \delta_j} K_{ij}$.

Optimal drug assignment with incomplete controllable microhabitats. Under complete control, the good enough strategy to minimize $\lambda_{\max}(A)$ is to assign a uniform drug distribution: $g_i = \langle g \rangle$ across all microhabitats. However, in practice, we may only be able to control a subset of microhabitats and apply high enough drug concentrations to push them to the maximum death rate d_0, while the remaining microhabitats stay approximately drug-free at growth rate g_0. In this scenario, the problem again becomes a discrete combinatorial optimization - selecting the optimal subcore.

When the number of controllable microhabitats is large, we should avoid targeting the well-connected core. Instead, we preserve this core (i.e., assign it positive growth rates), since through the kernel K, a well-connected node has large off-diagonal entries K_{ij} to many surrounding nodes, meaning its effective growth is strongly coupled to, and suppressed by, the drug-induced death at those surrounding "sink" nodes. Biologically, cells migrating away from the core into drug-saturated neighbours continuously remove individuals from the growing core population, as captured by the Laplacian term $-\beta L u$ in Eq. (1). In this precise sense, the connected core "senses" the surrounding sink landscape through network-mediated migration flux. Preserving this core at drug-free growth rate thus allows the network topology itself to suppress the population, rather than requiring additional drug at that site. The core can effectively "sense" the largest number of the surrounding "sink" microhabitats with maximum death rate d_0. Interestingly, when the number of controllable microhabitats is very limited-e.g., we can apply high drug concentration to only one node (setting $\delta_i = 0$)-we find that the optimal strategy is to suppress the microhabitat with the smallest K_{ii}, i.e., the node with the highest dynamic-related centrality (which often corresponds to highest degree). With more available microhabitats to control, we continue suppressing other nodes with high centralities in descending order.

Table 1 summarizes optimized strategies across different graph families based on this principle. For more complex structures, this centrality-based rule often provides a greedy but effective approximation of the optimal solution. However, to find the true optimal drug configuration, one still needs to solve the full discrete combinatorial problem of minimizing $\lambda(A_S)$ with partial control.

This drug assignment strategy under limited controllability is qualitatively similar to strategies used in epidemic outbreak suppression in susceptible-infectious-susceptible (SIS) network dynamics [49–52], where the optimal curing rate of each node is proportional to its degree. We note, however, that these two problems are not formally equivalent: SIS dynamics involve infection spreading between nodes, whereas our model involves population growth or decline at each node coupled by migration. The similarity is heuristic (both assign highest intervention priority to the most-connected nodes), but the underlying mathematical criteria differ. Thus, in our minimal growth-migration model: a. when many microhabitats are controllable, we protect the well-connected core; b. when only a few are controllable, we target the core to suppress it most effectively.

Robust population decline with unknown spatial drug heterogeneity. In most real-world scenarios, especially within the human body, estimating or controlling drug concentrations at each microhabitat is infeasible. Spatial drug heterogeneity is typically unknown (Fig 4A). Assuming we can estimate the migration rate β and control the total drug dose (or the spatially averaged growth rate $\langle g \rangle$), the problem becomes identifying robust clearance strategies that ensure population decline in the worst case. That is, we need:

$$\max \lambda_{\max}(A) < 1 \tag{6}$$

This is again a constrained optimization problem, which, as discussed earlier, reduces to selecting highly interconnected subcores (see S1 File, Section S6 for complete proof). To illustrate this framework across multi-microhabitat structures, we present migration-growth phase diagrams (β vs. $\langle g \rangle$) that identify parameter regimes yielding robust population decline under $\langle g \rangle < 0$. Besides robust population decline, population responses may still vary depending on heterogeneity, resulting in a "mixed phase" region where both growth and decline are possible. Note that for any $\langle g \rangle < 0$, the "even-spread" strategy always achieves decline, which means there's no region where robust population growth is possible.

For simplicity, we focus on the case where $g_0 \geq (N-1)\left|d_0\right|$, or equivalently $c \geq N$. Under this condition, which can be interpreted as the maximum drug-free growth rate being large relative to the death rate, the one-remainder strategy reduces to choosing a single growing microhabitat. Using the rank-1 structure of the resulting matrix A_S (see S1 File, Section S4.2 for the algebraic derivation), the condition $\max \lambda_{\max}(A) < 1$ simplifies exactly to: In this regime, the criterion:

$$\delta_r \cdot \max_i K_{ii} < 1 \tag{7}$$

Table 1. Optimized clearance strategies with limited controllable microhabitats, across different graph families based on the regularized Laplacian kernel matrix K. All entries are derived analytically from the closed-form K_{ii} expressions for each graph family (using $\gamma = \beta/|d_0|$ as the structural parameter) and have been numerically verified for $N = 10 - 40$ nodes and $\gamma \in [0.01, 10]$. Detailed derivations and physical intuition for each graph family are provided in S1 File, Section S8.

Graph family	Pattern of K_{ii}	Suppress first ($k=1$)	Suppress $k \ll N$ nodes
Path P_N	max at endpoints; min at centre	centre node $\lfloor N/2 \rfloor$	contiguous block centred in middle
Cycle C_N	all equal	any node (tie)	evenly spaced ($\approx N/k$ apart)
Star S_N	min at hub; max at leaves	hub	hub + (k–1) leaves
Clique K_N	all equal: $(1+\gamma)/(1+\gamma N)$	any node	any k nodes
d-regular grid	min in interior; max at boundary	most interior node	compact interior "hole"

https://doi.org/10.1371/journal.pcsy.0000113.t001

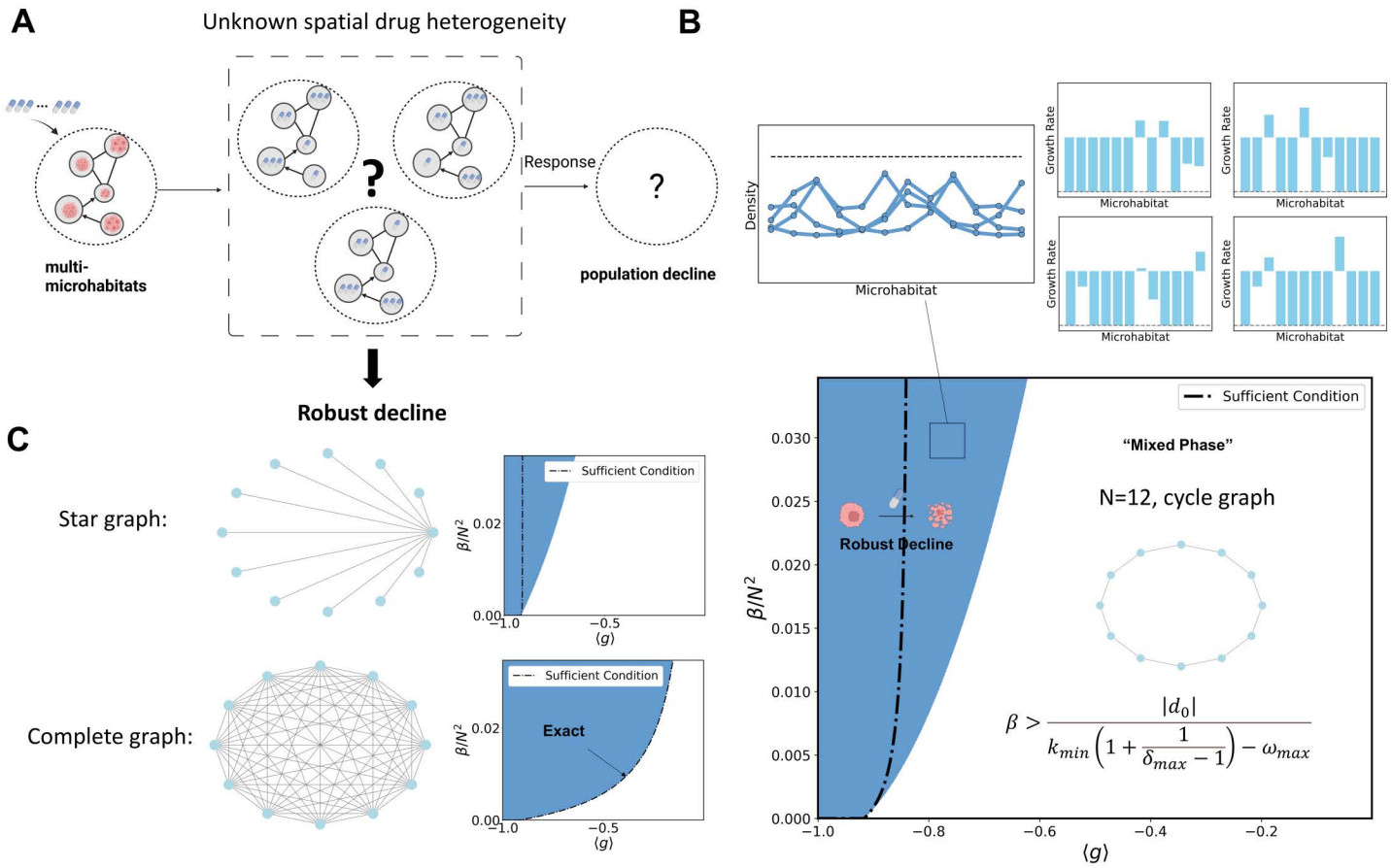

Fig 4. Robust population decline under unknown spatial drug heterogeneity. A. Illustration of the concept of robust population decline. When spatial drug heterogeneity is unknown, the clearance strategy evaluates whether population decline always occurs under a given migration rate and total drug dose, effectively eliminating the variability induced by different spatial drug configurations. **B.** Example phase diagram on a cycle graph, showing the relationship between migration rate β and spatially averaged growth rate $\langle g \rangle$. The bottom-right corner presents the mathematical form of the sufficient condition, which depends on β, maximum death rate d_0, minimum degree $k_{\min}$, maximum Laplacian eigenvalue $\omega_{\max}$, and maximum relative growth rate $\delta_{\max}$. Above the phase diagram, four final population densities after a finite time are shown for different spatial growth distributions selected from robust decline phase. The dashed line indicates the initial uniform population density. On the right, the corresponding spatial growth rate distributions are illustrated. **C.** Phase diagrams for two additional structures (star and complete graphs) under relatively high maximum growth rate $g_0 = 2(N-1)$ and low maximum death rate $d_0 = -1$. For the complete graph, the sufficient condition becomes exact, perfectly matching the numerical boundary. Icons created with BioRender.com [48].

https://doi.org/10.1371/journal.pcsy.0000113.g004

becomes an exact condition for robust population decline. Here, δ_r is the maximum possible relative growth rate, and $\max_i K_{ii}$ is the inverse dynamic-related centrality of the most isolated microhabitat. This condition tells us that as long as $\max_i K_{ii} < 1/\delta_r$, we are guaranteed robust population decline. Since $K_{ii} \propto \beta^{-1}$ and $\delta_r \propto \langle g \rangle$, this condition reveals a tradeoff: higher migration suppresses growth, while higher average growth promotes persistence. To better visualize this interplay, we apply an interpolation inequality to $\max_i K_{ii}$ and rearrange terms (see S1 File, Section S7.1), yielding a simplified analytical boundary for robust decline based only on structural extremes:

$$\beta > \frac{|d_0|}{k_{\min}\left(1 + \frac{1}{\delta_{\max}-1}\right) - \omega_{\max}} \tag{8}$$

Here, $k_{\min}$ is the minimum degree and $\omega_{\max}$ the largest Laplacian eigenvalue of the structure. We explicitly write $\delta_{\max} = \delta_r$ to emphasize its role as the extreme growth parameter. This bound clearly captures the fundamental tradeoff: to suppress populations with high intrinsic growth (δ_r), we need stronger inter-microhabitat migration (β). For a complete graph, where all nonzero Laplacian eigenvalues are equal, this inequality becomes exact (see S1 File, Section S7.1). In Fig 4B, we illustrate the phase diagram for a 12-node cycle graph. The blue region (top left) corresponds to robust decline $(\max \lambda_{\max}(A) < 1)$, while the white region represents the mixed phase. Our analytical bound provides a higher estimate for the true numerical boundary.

In cancer research, the star graph is especially relevant for modeling metastasis from a primary site to distant tissues [28,30]. Similarly, in bacterial communities, fully connected networks may arise [53,54]. Fig 4C presents phase diagrams for both star and complete graphs. In the complete graph (bottom panel), the sufficient condition precisely matches the numerical boundary.

For these two structures, we can derive closed-form expressions for $\max_i K_{ii}$. For star graph, the largest K_{ii} is at a leaf, and $(K_{ii})_{\text{leaf}} = \frac{1}{1+\gamma} + h \cdot \frac{\gamma^2}{(1+\gamma)^2}$, where $h = \frac{1}{1+\gamma(N-1)-\frac{\gamma^2(N-1)}{1+\gamma}}$, and $\gamma = \frac{\beta}{|d_0|}$ is the ratio of migration rate to maximum death rate. For complete graph, all nodes are identical, and $\max_i K_{ii} = \frac{1+\gamma}{1+\gamma N}$. Thus, for graphs like these, the boundary line can be exactly determined by solving $\delta_r \cdot \max_i K_{ii} = 1$. For more complex graphs where $\max_i K_{ii}$ is not analytically tractable (e.g., even cycles), our extreme-bound approximation from equation (8) still provides a fast and reliable method to identify regions of robust population decline.

Real-world application: colorectal cancer metastasis under systemic chemotherapy

To illustrate the practical utility of our framework, we apply it to a real-world cancer network motivated by clinical data. Colorectal cancer (CRC) is one of the most common metastatic cancers, and its primary organ-to-organ metastatic routes are well-characterised: cancer cells disseminate hematogenously and lymphatically from the primary colon tumour to the liver (via the portal vein), the lung (via systemic circulation), and regional lymph nodes [28,30]. This organotropic pattern defines a 4-node star network (hub = primary colon tumour; leaves = liver, lung, lymph node), precisely the topology for which our paper derives closed-form K_{ii} expressions (see Results).

We parameterise the model using published clinical measurements (Table 2). The drug-free tumour doubling time of CRC liver metastases is approximately 71 days [55], giving $g_0 \approx \ln 2/71 \approx 0.01\ \text{day}^{-1}$. We set $d_0 = -0.03\ \text{day}^{-1}$ $(|d_0|/g_0 = 3)$, representing the theoretical maximum death rate at saturating drug concentration. This ratio is consistent

Table 2. Parameter values for the CRC metastasis application under systemic chemotherapy. All organ-specific growth rates g_i are bounded by $[d_0, g_0]$. KG denotes the on-treatment tumour growth kinetics rate from Chen et al. 2024 [61]. Parameters marked "Modeling choice" are not directly extracted from a single source; see text for justification.

Parameter	Value	Derivation	Source
g_0 (drug-free growth rate)	$0.01\ \text{day}^{-1}$	$\ln 2/71$ days (CRC liver met doubling time)	Cucchetti et al. 2019 [55]
d_0 (max drug-induced death rate)	$-0.03\ \text{day}^{-1}$	Modeling choice: $\lvert d_0\rvert/g_0 = 3$; see text	–
β (inter-organ CTC colonisation rate)	$0.002\ \text{day}^{-1}$	Order-of-magnitude: CTC clearance × efficiency	Effective parameter; see text
g_{primary} (primary colon)	$-0.03\ \text{day}^{-1}$	$= d_0$; direct infusion, max drug	–
g_{liver} (liver metastasis)	$-0.015\ \text{day}^{-1}$	Modeling choice: strongest organ response	Zhou et al. 2021 [57]
g_{lung} (lung metastasis)	$+0.003\ \text{day}^{-1}$	On-treatment KG = $0.0202\ \text{wk}^{-1}$	Chen et al. 2024 [61]
g_{lymph} (lymph node metastasis)	$+0.002\ \text{day}^{-1}$	On-treatment KG = $0.0127\ \text{wk}^{-1}$	Chen et al. 2024 [61]
$\langle g \rangle$ (spatial average)	$-0.01\ \text{day}^{-1}$	$(-0.03 - 0.015 + 0.003 + 0.002)/4$	Derived
$\gamma = \beta/\lvert d_0\rvert$	0.067	Rescaled migration intensity	Derived

https://doi.org/10.1371/journal.pcsy.0000113.t002

with tumour growth inhibition models of mCRC, where the regression rate of drug-sensitive cells ($K_d \approx 0.017$ day^{-1}) exceeds the drug-free growth rate by a factor of ≈1.7 [56], and effective shrinkage-to-growth ratios of 3–6 are reported across mCRC chemotherapy trials [57]. The inter-organ CTC colonisation rate is estimated as $\beta \approx 0.002$ day^{-1}. This order-of-magnitude estimate is based on reported CTC half-lives of 1–2.4 hours in humans (clearance rate ≈ 8 day^{-1}) [58] combined with a colonisation efficiency of < 0.01% [59] (reviewed in [60]), yielding an effective seeding rate of order 10^{-3} day^{-1}. We note that β should be regarded as an effective model parameter, as no published compartmental model parameterises inter-organ bulk transfer in exactly this way.

Under standard mCRC chemotherapy, drug delivery is heterogeneous across organs [57]: the primary colon tumour receives maximum drug ($g_{\text{primary}} = d_0 = -0.03$); the liver, with high 5-fluorouracil first-pass extraction, shows the strongest response among metastatic sites (median nadir ratio 0.71 under chemotherapy alone [57]), and we set $g_{\text{liver}} = -0.015$ day^{-1} (intermediate between d_0 and 0). The lung and lymph node metastases show net-positive on-treatment growth, with organ-specific tumour growth kinetics $\text{KG}_{\text{lung}} = 0.0202$ wk^{-1} ≈ 0.003 day^{-1} and $\text{KG}_{\text{lymph}} = 0.0127$ wk^{-1} ≈ 0.002 day^{-1} [61]. Using KG as a proxy for g_i at these poorly-treated sites is defensible: KG in tumour growth inhibition models captures the net growth rate of lesions that progress despite ongoing chemotherapy, corresponding to the effective growth rate at organ sites where drug penetration is insufficient to achieve sustained regression. The spatially averaged growth rate is $\langle g \rangle = -0.01$ day^{-1} < 0, so by conventional drug-dose criteria the patient is in a treatment-response regime.

Applying our criterion (using the closed-form K_{ii} for a star graph), we find $\max_i K_{ii}\delta_i \approx 1.035 > 1$, indicating that, despite $\langle g \rangle < 0$, the population is predicted to *grow* rather than decline (Fig 5B). The lung microhabitat is the critical node: its on-treatment growth gives $\delta_{\text{lung}} = 1 + g_{\text{lung}}/|d_0| = 1.10$, and combined with its leaf $K_{ii} \approx 0.941$ (matching the analytical formula exactly), it drives $K_{ii}\delta_i \approx 1.035 > 1$. The lymph node is also near-critical ($K_{ii}\delta_i \approx 1.004$). To address the concern that these values lie close to the unity threshold, we computed both the exact largest eigenvalue $\lambda_{\max}(A) = 1.0353$ and a 10^4-sample Monte-Carlo sensitivity analysis over the published parameter ranges (S1 File, Section S9.1, Fig S5). The lower bound $\max_i K_{ii}\delta_i$ is tight to within 0.04% of $\lambda_{\max}(A)$ at this operating point, i.e., the higher-order corrections to the bound are negligible and the criterion can be read directly. Across the Monte-Carlo ensemble, $\lambda_{\max}(A) > 1$ in 76% of samples (median 1.06, 5%–95% percentile interval [0.92, 1.14]); the lung is identified as the dominant growth-driving microhabitat in 74% of samples and the lymph node in 64%. The remaining ∼ 24% of samples that fall below the unity threshold are concentrated in the upper end of the order-of-magnitude band on β, the dominant parameter uncertainty in the analysis. This means the lung acts as a growth reservoir that rescues the population despite the drug-induced death at other sites, a prediction that classical, spatially averaged dose-response analysis would miss entirely (it would predict decline based on $\langle g \rangle < 0$). To ensure robust decline, our framework prescribes improving lung drug delivery (reducing g_{lung} below ≈ 0.002 day^{-1}), which translates clinically to lung-targeted drug delivery strategies (e.g., inhaled or nanoparticle-delivered chemotherapy). Equivalently, increasing the rescaled migration intensity $\gamma = \beta/|d_0|$ above ≈0.11 pushes $\max_i K_{ii}\delta_i$ below 1, which is a necessary condition for population decline; further increasing γ until the upper bound $\max_i \sum_j \sqrt{\delta_i \delta_j} K_{ij}$ also drops below 1 guarantees decline (Fig 5D). We note that the star topology is a first-order approximation; secondary metastasis from liver to lung (cascade seeding) has been documented in CRC [28] and could be incorporated by adding a directed liver-to-lung edge, though this would break the star symmetry and require numerical rather than analytical K_{ii} computation. This prediction is consistent with clinical data showing that approximately 60% of mCRC patients exhibit at least one metastatic lesion responding contrarily from the total tumour burden, with liver lesions showing the strongest response and lung lesions the weakest under chemotherapy [57].

A second simplification, beyond the first-order star topology, is that the inter-organ Laplacian L is taken to be symmetric: primary-to-leaf and leaf-to-primary effective transit rates are equal. This is a modelling convenience; biologically, hematogenous and lymphatic dissemination from the primary colon tumour to metastatic sites is well-characterised, whereas reverse "self-seeding" from metastatic back to primary sites is rarely observed in CRC and not quantitatively constrained

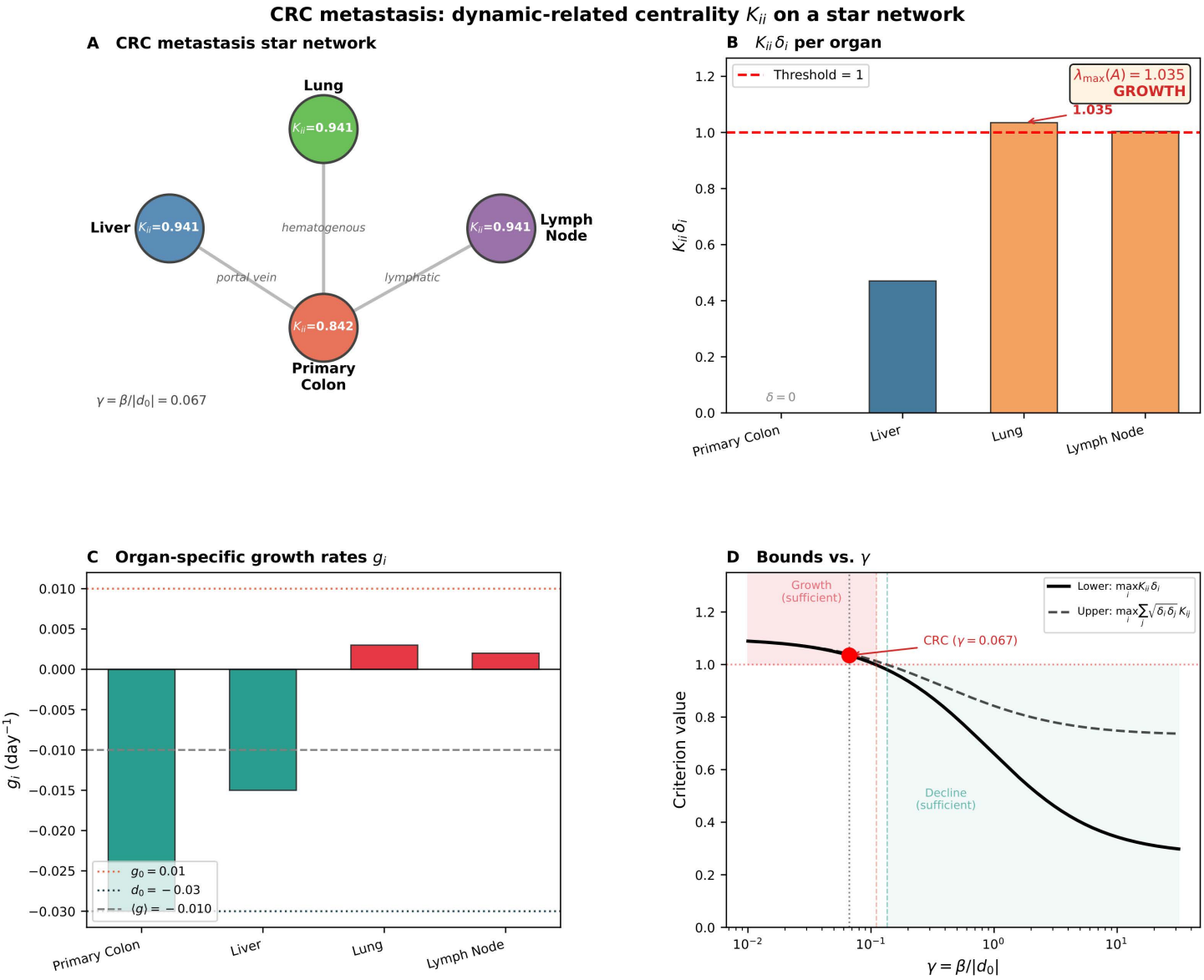

Fig 5. Real-world application: colorectal cancer (CRC) metastasis under systemic chemotherapy, modelled as a 4-node star network. A. Star network: primary colon tumour (hub) connected to liver, lung, and lymph node (leaves) via hematogenous and lymphatic routes. Node colour distinguishes organs; K_{ii} values are shown on each node. The rescaled migration intensity $\gamma = \beta/|d_0| = 0.067$. **B.** Bar chart of $K_{ii}\delta_i$ per organ. The dashed red line marks the threshold $K_{ii}\delta_i = 1$. The lung exceeds this threshold ($K_{ii}\delta_i \approx 1.035 > 1$), predicting population growth despite $\langle g \rangle < 0$. **C.** Organ-specific growth rates g_i (see Table 2 for sources). Dotted lines indicate g_0 and d_0; the dashed grey line shows $\langle g \rangle = -0.01$ day^{-1}. **D.** Sensitivity of population response bounds to γ. Solid black curve: lower bound $\max_i K_{ii}\delta_i$ (above 1 = sufficient for growth). Dashed black curve: upper bound $\max_i \sum_j \sqrt{\delta_i \delta_j} K_{ij}$ (below 1 = sufficient for decline). Between the two critical γ values where each bound crosses 1, the outcome depends on the specific spatial arrangement. The red dot marks the CRC operating point ($\gamma = 0.067$), where the lower bound exceeds 1 and growth is predicted. See Table 2 for all parameter values.

https://doi.org/10.1371/journal.pcsy.0000113.g005

[62,63]. Our framework accommodates asymmetric transport by replacing L with a directed counterpart; the kernel $K = (I + \gamma L)^{-1}$ remains well-defined for general L. To check that the symmetric simplification does not change our qualitative conclusion, we swept the asymmetry parameter ε = (reverse rate)/(forward rate) from $\varepsilon = 1$ (the symmetric model) to

$\varepsilon = 0$ (the empirical CRC limit of negligible reverse seeding) and recomputed $K_{ii}\delta_i$ for each organ (S1 File, Section S9.2, Fig S6). The lung's $K_{ii}\delta_i$ increases monotonically from 1.035 (symmetric) to 1.100 (asymmetric limit), and the lymph node's increases from 1.004 to 1.067; both remain above unity across the entire range. Intuitively, the symmetric model implicitly allows leaf-grown cells to migrate back to the primary tumour where they die ($g_{\text{primary}} = d_0 < 0$), so it underestimates the lung's contribution to growth; closing this loss channel under realistic asymmetry strengthens the prediction. The qualitative finding (lung as the critical growth reservoir) is therefore robust to, and indeed strengthened by, directional asymmetry in CRC dissemination, although a full numerical exploration of asymmetric L parameterised by experimentally or clinically measured directional inter-organ transport rates is left to future work.

Discussion

Complex biological systems, such as cancer and bacterial populations, are deeply intertwined with network structure, growth dynamics, and spatial interactions. In this study, we introduced a kernel transformation that enabled the derivation of a new theoretical criterion predicting population-level responses across arbitrary multi-microhabitat structures under spatially heterogeneous drug environments. This transformation naturally links population dynamics to a centrality measure known as forest closeness centrality, which we refer to as *dynamic-related centrality* in our framework. Our findings demonstrate that increasing connectivity between microhabitats consistently promotes population decline, effectively mimicking the impact of increasing the migration rate. Furthermore, we show that the optimization of spatial drug heterogeneity for inducing population decline can be reduced to a subgraph selection problem on the transformed fully connected graph. In addition, we identify a parameter regime in the growth-migration phase diagram that supports robust population decline, i.e., a guaranteed clearance across all spatial drug configurations if the actual spatial drug heterogeneity is unknown. We derive a sufficient theoretical condition characterizing this phase, capturing the interplay between spatially averaged growth and migration rates. Notably, this condition becomes exact when the underlying microhabitat structure is a complete graph.

In [23], perturbation approximation was successfully applied to derive an analytical expression for the largest eigenvalue $\lambda_{\max}(G-\beta L)$, where $L = \frac{\partial^2}{\partial x^2}$ is the Laplacian operator with two absorbing boundaries on a one-dimensional continuous space. The key reason perturbation theory succeeds in the continuous case but fails in the discrete multi-microhabitat case is the presence of absorbing boundaries: in 1D, the unperturbed largest eigenvector of L already encodes boundary effects, giving non-uniform spatial importance to different positions. In our discrete setting, when L is the graph Laplacian of an undirected connected graph, the unperturbed eigenvector is uniform ($u_0 \propto \mathbf{1}$), so first-order perturbation theory returns only the spatially averaged growth rate $\langle g \rangle$ and fails to distinguish spatial arrangements. The approximated form revealed two optimized strategies for spatial drug arrangement by examining the unperturbed largest eigenvector of L: the "importance" of spatial positions is ranked by the squared components of this eigenvector. And it's found that, assigning drug-free growth rates g_0 to central positions tends to mitigate population decline, while assigning g_0 near absorbing boundaries tends to accelerate it. However, when the spatial structure becomes discrete, and the driving force of decline arises not from absorbing boundaries, but from "sink" microhabitats with negative growth rates (We distinguish "absorbing boundaries" (in 1D continuous models), where population density is forced to zero at domain boundaries so that cells reaching the boundary are permanently lost, from "sink microhabitats" (in our discrete model), which are nodes with gi < 0 that remove cells through drug-induced death rather than boundary absorption.), perturbation theory fails to accurately capture the system's behavior; it reflects only the effect of spatially averaged growth. In contrast, our kernel transformation introduces a new matrix $A = D^{1/2}KD^{1/2}$, where $K = (I + \gamma L)^{-1}$ is the regularized Laplacian kernel and D is the diagonal matrix of growth-related weights. Even first-order perturbation theory fails on K, since K and L share the same eigenbasis, and thus the largest eigenvector still assigns equal importance to all microhabitats.

Despite this, the diagonal elements K_{ii}, which correspond to forest closeness centrality (or what we refer to as "dynamic-related centrality") provide a meaningful measure for ranking the relative importance of microhabitats. Although

perturbation theory is insufficient in this setting, the kernel matrix K still allows us to heuristically infer microhabitat importance and guide spatial drug dosing strategies. In particular, it enables a greedy subcore selection strategy on the transformed fully connected graph, as discussed in the main text. This insight allows us to extend the one-dimensional intuition: assigning g_0 to central or boundary positions depends on the controllability context. In our discrete framework, the "center" corresponds to a well-interconnected core, while the "edges" represent relatively isolated subgraphs. Thus, through kernel transformation, we heuristically recover spatial clearance strategies based on dynamic-related centralities, even in cases where classical perturbation methods break down.

Across-node properties such as centrality measures play a crucial role in graph theory and network analysis. For instance, subgraph centrality quantifies node importance based on participation in subgraphs [64], with a bias toward smaller subgraphs. Interestingly, our dynamic-related centrality C exhibits a similar relationship with traditional closeness centrality, correlating with node degree, and other centrality measures such as Katz or eigenvalue centrality [65,66]. Recent work on dynamic centrality has aimed to integrate topological and dynamical properties of nodes to identify influential spreaders [67–70]. For example, Grindrod et al. [68] define communicability-based centrality on time-varying networks, and Poulin et al. [67] weight node importance by local spreading dynamics. However, these previous formulations of dynamic centrality primarily focus on the addition or deletion of nodes within a network; they remain fundamentally structural measures that describe the dynamics of the network itself. In contrast, our dynamic-related centrality focuses on predicting the results of dynamics occurring on the network, and it naturally emerges from the dynamics itself by doing the kernel transformation. This distinction makes our proposed measure novel, and we term it "dynamic-related centrality" to distinguish it from "dynamic centrality" for the dynamics of the network. We anticipate that this new centrality will expand existing centrality classifications and provide direct insights into dynamic properties without requiring complex simulations. Interestingly, our matrix K, which defines the dynamic-related centrality C, shares the same mathematical form as the classical regularized Laplacian kernel (RLK) [71], a well-known graph similarity measure based on the Laplacian matrix L. Despite this shared mathematical form, we emphasize important conceptual differences. First, in our growth-migration framework, the parameter $\gamma = \frac{\beta}{|d_0|}$ arises naturally from the underlying population dynamics, rather than being introduced as a free parameter. Second, while the RLK is typically used to analyze off-diagonal elements to quantify node-to-node similarity, our analysis centers on the diagonal entries K_{ii}, which correspond to forest closeness centrality and reflect the self-centrality of each node in the dynamic context (While $\lambda_{\max}(A)$ can be interpreted through a walk-based perspective, capturing contributions from paths traversing multiple nodes thus considering interactions between different nodes; this interpretation is beyond the scope of the present work and is not central to our theoretical framework). Establishing these connections between our dynamic-related centrality and classical graph-theoretic measures not only enhances the interpretability of our framework but also expands its potential applications in network-based modeling of biological systems.

In the main text, we did not emphasize the upper bound $\lambda_{\max}(A) \leq \max_i \sum_j \sqrt{\delta_i \delta_j} K_{ij}$, which not only serves as a useful heuristic for guiding optimized drug allocation strategies, but also reveals deeper structural insights. Specifically, we find that this maximum row sum is tightly linked to the presence of local symmetries in the system. When the matrix A, or a principal submatrix $A[S]$, is circulant, the inequality becomes an equality: $\lambda_{\max}(A) = \max_i \sum_j \sqrt{\delta_i \delta_j} K_{ij}$. Although spatial drug heterogeneity generally breaks most global symmetries in the underlying structure, certain local symmetries may still be preserved. In such cases, this equality offers a convenient and accurate method for predicting population response by directly evaluating the maximum row sum of A. Detailed derivations, along with illustrative examples, are provided in S1 File.

Understanding population responses to drug treatment, such as antibiotics or chemotherapy, is critical for assessing therapeutic success. Recent studies in both bacterial and cancer systems have identified an interesting phenomenon known as "bistability", where small differences in key parameters, such as drug concentration or growth rate, can lead to drastically different outcomes [72–76]. This concept helps explain variability in clinical outcomes. Here, we propose an alternative explanation for the observed variability in patient treatment outcomes: spatial drug heterogeneity and

differences in microhabitat connectivity may produce two qualitatively distinct outcomes (growth or decline) even under the same total drug dose and without requiring bistability. Specifically, our framework predicts that small changes in connectivity or drug spatial distribution near the $\lambda_{max}(A) = 1$ boundary can flip the population outcome from growth to decline, providing a network-level mechanism for the clinically observed heterogeneity in treatment response. Indeed, large-cohort studies of mCRC report that approximately 60% of patients exhibit at least one metastatic lesion responding contrarily from the total tumour burden [57], consistent with such spatial heterogeneity effects. This insight could inform the development of new treatment strategies tailored to spatial drug distribution patterns.

A critical caveat to the finding that higher connectivity promotes population decline is that connectivity can simultaneously act as a *therapeutic challenge*. In bacterial populations, antibiotic-resistant variants can share resistance genes with susceptible neighbours through horizontal gene transfer and plasmid conjugation; higher connectivity may therefore accelerate the spread of resistance and cause the drug to lose its effect over evolutionary time [77]. In cancer, emerging evidence suggests that circulating tumour cell (CTC) clusters, groups of co-migrating cells that exploit the same hematogenous routes modelled here, show dramatically higher metastatic efficiency than single CTCs [78–80]. These cooperative metastatic clusters can "carry" cells that would not survive alone, exploiting high-connectivity routes in a way our current model does not capture. Our framework therefore addresses a single aspect of connectivity's role: its short-term effect on population-level growth/decline dynamics under fixed drug treatment, assuming no resistance evolution and no cooperative migration. Extending the model to incorporate evolutionary dynamics or cooperative CTC migration remains an important direction for future work.

Experimental studies have demonstrated the impact of spatial structure on growth [23,81], competition, and evolution [82–85]. Our theoretical findings may aid in the interpretation of experimental results and guide the design of future studies. Combining theoretical and experimental approaches can enhance our understanding and contribute to the development of spatially explicit drug dosing strategies.

The migration rate β in our model represents the per-cell rate of density-independent dispersal between connected microhabitats, applicable to both passive diffusion-like processes and constant-rate active motility. For bacterial systems, experimentally measured values range from $\sim 10^{-3}$ h^{-1} for passive diffusion in agar [13] to $\sim 10^{-2}$ h^{-1} for motile strains [11]. For the CRC cancer metastasis example, we estimated $\beta \approx 0.002$ day^{-1} as a conservative estimate of CTC colonisation efficiency (see Table 2). We note that while the core criterion $\lambda_{max}(A) < 1$ and the kernel transformation remain valid for general (possibly asymmetric) graph Laplacians, the closed-form K_{ii} expressions presented here focus on the undirected (symmetric) case. Active, directed migration (e.g., chemotaxis in bacteria, or epithelial-mesenchymal transition-driven invasion in cancer) can be modelled within our framework using an asymmetric L; we have illustrated this for the CRC application in S1 File, Section S9.2, where the qualitative prediction is preserved across the full range from symmetric to fully asymmetric inter-organ transport. Extending this analysis to other biological systems with experimentally measured directional rates is a natural direction for future work.

This study explored population responses across various microhabitat structures and spatial drug heterogeneities, revealing insights beyond previous research that primarily focused on homogeneous structures and drug distributions. However, several limitations warrant explicit discussion.

First, our model uses a linearised (exponential) growth equation, which ignores density-dependent competition and carrying capacity. This approximation is appropriate for the early-time, short-term population response, the regime where the question of growth versus decline is decided. However, it means our predictions are not applicable to long-term steady-state behaviour, where logistic or competitive dynamics become important [39]. Second, we assume a static drug distribution fixed in space and time. In practice, drug concentrations evolve due to diffusion, metabolism, and pharmacokinetics; temporal drug fluctuations could shift the effective $\{g_i\}$ and alter the predicted phase boundary [14]. Third, the microhabitat network topology is assumed static, whereas real biological structures (tumour vasculature, biofilm architecture, metastatic sites) evolve during treatment. Fourth, we consider a single cell type without frequency-dependent growth

or interspecies interactions; multi-species extensions using evolutionary game theory [86,87] are a natural future direction. Finally, the main text uses canonical graph families (path, cycle, star, complete) for analytical tractability, and S1 File demonstrates the framework on the Zachary Karate Club network (34 nodes); applying the framework to larger biological networks (e.g., scale-free tumour vasculature, biofilm architectures) is computationally straightforward (requiring only an $N \times N$ matrix inversion) but remains to be explored with real topological data.

Despite these limitations, the framework provides a rigorous analytical benchmark: it identifies the conditions under which spatial drug heterogeneity is or is not sufficient to rescue a population from an overall decline regime, and provides computationally efficient criteria that can be applied without full eigenvalue calculations.

Supporting information

S1 File. Supplementary Information. Expanded descriptions of mathematical models, details of population decline criterion derivations, and 9 supplemental figures.
(PDF)

Acknowledgments

We sincerely thank Dr. David Lubensky and Dr. Michal Zochowski for insightful discussions. Dr. Kevin Wood passed away before the completion of this manuscript. Zhijian Hu accepts responsibility for the integrity and validity of the analyses and results presented.

Author contributions

Conceptualization: Zhijian Hu, Kevin Wood.

Formal analysis: Zhijian Hu.

Funding acquisition: Kevin Wood.

Investigation: Zhijian Hu.

Methodology: Zhijian Hu.

Software: Zhijian Hu.

Supervision: Kevin Wood.

Validation: Zhijian Hu.

Visualization: Zhijian Hu.

Writing – original draft: Zhijian Hu.

Writing – review & editing: Zhijian Hu.

References

1. Wood K. Microbial Ecology: Complex Bacterial Communities Reduce Selection for Antibiotic Resistance. Curr Biol. 2019;29(21):R1143–5. https://doi.org/10.1016/j.cub.2019.09.017 PMID: 31689403
2. Denk-Lobnig M, Wood KB. Antibiotic resistance in bacterial communities. Curr Opin Microbiol. 2023;74:102306.
3. Aguadé-Gorgorió G, Anderson ARA, Solé R. Modeling tumors as complex ecosystems. iScience. 2024;27(9):110699. https://doi.org/10.1016/j.isci.2024.110699 PMID: 39280631
4. Hansen E, Karslake J, Woods RJ, Read AF, Wood KB. Antibiotics can be used to contain drug-resistant bacteria by maintaining sufficiently large sensitive populations. PLoS Biol. 2020;18(5):e3000713. https://doi.org/10.1371/journal.pbio.3000713 PMID: 32413038
5. Gallaher JA, Enriquez-Navas PM, Luddy KA, Gatenby RA, Anderson AR. Spatial heterogeneity and evolutionary dynamics modulate time to recurrence in continuous and adaptive cancer therapies. Cancer Res. 2018;78(8):2127–39.

6. West J, Adler F, Gallaher J, Strobl M, Brady-Nicholls R, Brown J, et al. A survey of open questions in adaptive therapy: Bridging mathematics and clinical translation. Elife. 2023;12:e84263. https://doi.org/10.7554/eLife.84263 PMID: 36952376
7. Strobl MA, Martin AL, West J, Gallaher J, Robertson-Tessi M, Gatenby R, et al. To modulate or to skip: De-escalating parp inhibitor maintenance therapy in ovarian cancer using adaptive therapy. Cell Syst. 2024;15(6):510–25.
8. Gallagher K, Strobl MA, Park DS, Spoendlin FC, Gatenby RA, Maini PK, et al. Mathematical model-driven deep learning enables personalized adaptive therapy. Cancer Res. 2024;84(11):1929–41.
9. Chakraborty PP, Nemzer LR, Kassen R. Experimental evidence that metapopulation structure can accelerate adaptive evolution. BioRxiv. 2021;:2021–07.
10. Wu A, Loutherback K, Lambert G, Estévez-Salmerón L, Tlsty TD, Austin RH, et al. Cell motility and drug gradients in the emergence of resistance to chemotherapy. Proc Natl Acad Sci U S A. 2013;110(40):16103–8. https://doi.org/10.1073/pnas.1314385110 PMID: 24046372
11. Baym M, Lieberman TD, Kelsic ED, Chait R, Gross R, Yelin I, et al. Spatiotemporal microbial evolution on antibiotic landscapes. Science. 2016;353(6304):1147–51. https://doi.org/10.1126/science.aag0822 PMID: 27609891
12. Hermsen R, Hwa T. Sources and sinks: a stochastic model of evolution in heterogeneous environments. Phys Rev Lett. 2010;105(24):248104.
13. Hermsen R, Deris JB, Hwa T. On the rapidity of antibiotic resistance evolution facilitated by a concentration gradient. Proc Natl Acad Sci U S A. 2012;109(27):10775–80. https://doi.org/10.1073/pnas.1117716109 PMID: 22711808
14. Xie H, Jiao Y, Fan Q, Hai M, Yang J, Hu Z, et al. Modeling three-dimensional invasive solid tumor growth in heterogeneous microenvironment under chemotherapy. PLoS One. 2018;13(10):e0206292. https://doi.org/10.1371/journal.pone.0206292 PMID: 30365511
15. Piskovsky V, Oliveira NM. Bacterial motility can govern the dynamics of antibiotic resistance evolution. Nat Commun. 2023;14(1):5584.
16. Marrec L, Lamberti I, Bitbol AF. Toward a universal model for spatially structured populations. Phys Rev Lett. 2021;127(21):218102.
17. De Jong MG, Wood KB. Tuning spatial profiles of selection pressure to modulate the evolution of drug resistance. Phys Rev Lett. 2018;120(23):238102.
18. Zhang Q, Lambert G, Liao D, Kim H, Robin K, Tung CK, et al. Acceleration of emergence of bacterial antibiotic resistance in connected microenvironments. Science. 2011;333(6050):1764–7.
19. De Jong M. Emergence of antibiotic resistance in microbial populations with spatial heterogeneity. PhD thesis. University of Michigan; 2021.
20. Lamont JT. Patient education: Helicobacter pylori infection and treatment (beyond the basics). 2022.
21. Dent R, Trudeau M, Pritchard KI, Hanna WM, Kahn HK, Sawka CA, et al. Triple-negative breast cancer: clinical features and patterns of recurrence. Clin Cancer Res. 2007;13(15):4429–34.
22. Riggio AI, Varley KE, Welm AL. The lingering mysteries of metastatic recurrence in breast cancer. Br J Cancer. 2021;124(1):13–26.
23. Hu Z, Wu Y, Freire T, Gjini E, Wood K. Linking spatial drug heterogeneity to microbial growth dynamics in theory and experiment. PLoS Comput Biol. 2026;22(1):e1013896. https://doi.org/10.1371/journal.pcbi.1013896 PMID: 41557766
24. Freire TFA, Hu Z, Wood KB, Gjini E. Modeling spatial evolution of multi-drug resistance under drug environmental gradients. PLoS Comput Biol. 2024;20(5):e1012098. https://doi.org/10.1371/journal.pcbi.1012098 PMID: 38820350
25. Chen LL, Blumm N, Christakis NA, Barabási A-L, Deisboeck TS. Cancer metastasis networks and the prediction of progression patterns. Br J Cancer. 2009;101(5):749–58. https://doi.org/10.1038/sj.bjc.6605214 PMID: 19707203
26. Budczies J, von Winterfeld M, Klauschen F, Bockmayr M, Lennerz JK, Denkert C, et al. The landscape of metastatic progression patterns across major human cancers. Oncotarget. 2014;6(1):570.
27. Costa L da F, Oliveira ON Jr, Travieso G, Rodrigues FA, Villas Boas PR, Antiqueira L, et al. Analyzing and modeling real-world phenomena with complex networks: a survey of applications. Adv Phys. 2011;60(3):329–412. https://doi.org/10.1080/00018732.2011.572452
28. Riihimäki M, Hemminki A, Fallah M, Thomsen H, Sundquist K, Sundquist J, et al. Metastatic sites and survival in lung cancer. Lung Cancer. 2014;86(1):78–84.
29. Riihimäki M, Thomsen H, Sundquist K, Sundquist J, Hemminki K. Clinical landscape of cancer metastases. Cancer Med. 2018;7(11):5534–42.
30. Jin X, Demere Z, Nair K, Ali A, Ferraro GB, Natoli T, et al. A metastasis map of human cancer cell lines. Nature. 2020;588(7837):331–6. https://doi.org/10.1038/s41586-020-2969-2 PMID: 33299191
31. Trevaskis NL, Kaminskas LM, Porter CJ. From sewer to saviour—targeting the lymphatic system to promote drug exposure and activity. Nat Rev Drug Discov. 2015;14(11):781–803.
32. Kodama T, Matsuki D, Tada A, Takeda K, Mori S. New concept for the prevention and treatment of metastatic lymph nodes using chemotherapy administered via the lymphatic network. Sci Rep. 2016;6:32506. https://doi.org/10.1038/srep32506 PMID: 27581921
33. Ji H, Hu C, Yang X, Liu Y, Ji G, Ge S, et al. Lymph node metastasis in cancer progression: molecular mechanisms, clinical significance and therapeutic interventions. Signal Transduct Target Ther. 2023;8(1):367.
34. Wheatley RM, Caballero JD, van der Schalk TE, De Winter FHR, Shaw LP, Kapel N, et al. Gut to lung translocation and antibiotic mediated selection shape the dynamics of Pseudomonas aeruginosa in an ICU patient. Nat Commun. 2022;13(1):6523. https://doi.org/10.1038/s41467-022-34101-2 PMID: 36414617

35. Ziaka M, Exadaktylos A. Exploring the lung-gut direction of the gut-lung axis in patients with ARDS. Crit Care. 2024;28(1):179. https://doi.org/10.1186/s13054-024-04966-4 PMID: 38802959
36. Eladham MW, Selvakumar B, Sharif-Askari NS, Sharif-Askari FS, Ibrahim SM, Halwani R. Unraveling the gut-lung axis: Exploring complex mechanisms in disease interplay. Heliyon. 2024.
37. Lee AJ, Wang S, Meredith HR, Zhuang B, Dai Z, You L. Robust, linear correlations between growth rates and β-lactam-mediated lysis rates. Proc Natl Acad Sci U S A. 2018;115(16):4069–74. https://doi.org/10.1073/pnas.1719504115 PMID: 29610312
38. Pearl Mizrahi S, Goyal A, Gore J. Community interactions drive the evolution of antibiotic tolerance in bacteria. Proc Natl Acad Sci U S A. 2023;120(3):e2209043119. https://doi.org/10.1073/pnas.2209043119 PMID: 36634144
39. Bren A, Glass DS, Kohanim YK, Mayo A, Alon U. Tradeoffs in bacterial physiology determine the efficiency of antibiotic killing. Proc Natl Acad Sci U S A. 2023;120(51):e2312651120. https://doi.org/10.1073/pnas.2312651120 PMID: 38096408
40. Geyrhofer L, Ruelens P, Farr AD, Pesce D, de Visser JAGM, Brenner N. Minimal Surviving Inoculum in Collective Antibiotic Resistance. mBio. 2023;14(2):e0245622. https://doi.org/10.1128/mbio.02456-22 PMID: 37022160
41. Quinn K, Terzi E, Crovella M. Characterizing Covid Waves via Spatio-Temporal Decomposition. In: Proceedings of the 28th ACM SIGKDD Conference on Knowledge Discovery and Data Mining. 2022. p. 3783–91.
42. Aziz F, Slater LT, Bravo-Merodio L, Acharjee A, Gkoutos GV. Link prediction in complex network using information flow. Sci Rep. 2023;13(1):14660.
43. Huang L, Liao L, Wu CH. Protein-protein interaction prediction based on multiple kernels and partial network with linear programming. BMC Systems Biology. 2016;10:151–64.
44. Fan J, Cannistra A, Fried I, Lim T, Schaffner T, Crovella M, et al. Functional protein representations from biological networks enable diverse cross-species inference. Nucleic Acids Res. 2019;47(9):e51. https://doi.org/10.1093/nar/gkz132 PMID: 30847485
45. Ray S, Lall S, Bandyopadhyay S. A Deep Integrated Framework for Predicting SARS-CoV2–Human Protein-Protein Interaction. IEEE Trans Emerg Top Comput Intell. 2022;6(6):1463–72. https://doi.org/10.1109/tetci.2022.3182354
46. Jin Y, Bao Q, Zhang Z. Forest distance closeness centrality in disconnected graphs. In: 2019 IEEE International Conference on Data Mining (ICDM). 2019. p. 339–48.
47. van der Grinten A, Angriman E, Predari M, Meyerhenke H. New Approximation Algorithms for Forest Closeness Centrality – for Individual Vertices and Vertex Groups. Proceedings of the 2021 SIAM International Conference on Data Mining (SDM). Society for Industrial and Applied Mathematics; 2021. p. 136–44.
48. Hu Z, Wood K. Figures created with BioRender. BioRender.com. Published with a BioRender Academic Publication License. 2025.
49. Ferreira SC, Castellano C, Pastor-Satorras R. Epidemic thresholds of the susceptible-infected-susceptible model on networks: A comparison of numerical and theoretical results. Phys Rev E Stat Nonlin Soft Matter Phys. 2012;86(4):041125.
50. Li C, van de Bovenkamp R, Van Mieghem P. Susceptible-infected-susceptible model: A comparison of n-intertwined and heterogeneous mean-field approximations. Phys Rev E Stat Nonlin Soft Matter Phys. 2012;86(2):026116.
51. Cator E, Van Mieghem P. Susceptible-infected-susceptible epidemics on the complete graph and the star graph: Exact analysis. Phys Rev E Stat Nonlin Soft Matter Phys. 2013;87(1):012811.
52. Chen H, Li G, Zhang H, Hou Z. Optimal allocation of resources for suppressing epidemic spreading on networks. Phys Rev E. 2017;96(1–1):012321. https://doi.org/10.1103/PhysRevE.96.012321 PMID: 29347176
53. Pearce MT, Agarwala A, Fisher DS. Stabilization of extensive fine-scale diversity by ecologically driven spatiotemporal chaos. Proc Natl Acad Sci U S A. 2020;117(25):14572–83. https://doi.org/10.1073/pnas.1915313117 PMID: 32518107
54. Hu J. Emergent behaviors in complex microbial ecosystems. PhD thesis. Massachusetts Institute of Technology; 2024.
55. Cucchetti A, Russolillo N, Johnson P, Tarchi P, Ferrero A, Cucchi M, et al. Impact of primary cancer features on behaviour of colorectal liver metastases and survival after hepatectomy. BJS Open. 2018;3(2):186–94. https://doi.org/10.1002/bjs5.100 PMID: 30957066
56. Zhou J, Cipriani A, Liu Y, Fang G, Li Q, Cao Y. Mapping lesion-specific response and progression dynamics and inter-organ variability in metastatic colorectal cancer. Nat Commun. 2023;14(1):515.
57. Zhou J, Li Q, Cao Y. Spatiotemporal Heterogeneity across Metastases and Organ-Specific Response Informs Drug Efficacy and Patient Survival in Colorectal Cancer. Cancer Res. 2021;81(9):2522–33. https://doi.org/10.1158/0008-5472.CAN-20-3665 PMID: 33589516
58. Hamza B, Ng SR, Prakadan SM, Delgado FF, Chin CR, King EM, et al. Optofluidic real-time cell sorter for longitudinal CTC studies in mouse models of cancer. Proc Natl Acad Sci U S A. 2019;116(6):2232–6. https://doi.org/10.1073/pnas.1814102116 PMID: 30674677
59. Luzzi KJ, MacDonald IC, Schmidt EE, Kerkvliet N, Morris VL, Chambers AF, et al. Multistep nature of metastatic inefficiency: dormancy of solitary cells after successful extravasation and limited survival of early micrometastases. Am J Pathol. 1998;153(3):865–73.
60. Chaffer CL, Weinberg RA. A perspective on cancer cell metastasis. Science. 2011;331(6024):1559–64. https://doi.org/10.1126/science.1203543 PMID: 21436443
61. Chen C, Feng YS, Wang Z, Gupta M, Xu XS, Yan X. Organ-specific tumor dynamics predict survival of patients with metastatic colorectal cancer. Eur J Cancer. 2024;207:114147. https://doi.org/10.1016/j.ejca.2024.114147 PMID: 38834016

62. Kim M-Y, Oskarsson T, Acharyya S, Nguyen DX, Zhang XH-F, Norton L, et al. Tumor self-seeding by circulating cancer cells. Cell. 2009;139(7):1315–26. https://doi.org/10.1016/j.cell.2009.11.025 PMID: 20064377
63. Comen E, Norton L, Massagué J. Clinical implications of cancer self-seeding. Nat Rev Clin Oncol. 2011;8(6):369–77.
64. Estrada E, Rodriguez-Velazquez JA. Subgraph centrality in complex networks. Physical Review E—Statistical, Nonlinear, and Soft Matter Physics. 2005;71(5):056103.
65. Katz L. A New Status Index Derived from Sociometric Analysis. Psychometrika. 1953;18(1):39–43. https://doi.org/10.1007/bf02289026
66. Newman ME. The mathematics of networks. The new palgrave encyclopedia of economics. vol. 2. 2008. p. 1–12.
67. Poulin R, Boily MC, Msse BR. Dynamical systems to define centrality in social networks. Soc Netw. 2000;22(3):187–220.
68. Grindrod P, Higham DJ. A dynamical systems view of network centrality. Proc Math Phys Eng Sci. 2014;470(2165):20130835. https://doi.org/10.1098/rspa.2013.0835 PMID: 24808758
69. Liu J-G, Lin J-H, Guo Q, Zhou T. Locating influential nodes via dynamics-sensitive centrality. Sci Rep. 2016;6(1):21380.
70. Huang DW, Yu ZG. Dynamic-sensitive centrality of nodes in temporal networks. Sci Rep. 2017;7(1):41454.
71. Smola AJ, Kondor R. Kernels and regularization on graphs. In: Learning Theory and Kernel Machines: 16th Annual Conference on Learning Theory and 7th Kernel Workshop, COLT/Kernel 2003, Washington, DC, USA, August 24-27, 2003. Proceedings. 2003. p. 144–58.
72. Dai L, Vorselen D, Korolev KS, Gore J. Generic indicators for loss of resilience before a tipping point leading to population collapse. Science. 2012;336(6085):1175–7. https://doi.org/10.1126/science.1219805 PMID: 22654061
73. Karslake J, Maltas J, Brumm P, Wood KB. Population Density Modulates Drug Inhibition and Gives Rise to Potential Bistability of Treatment Outcomes for Bacterial Infections. PLoS Comput Biol. 2016;12(10):e1005098. https://doi.org/10.1371/journal.pcbi.1005098 PMID: 27764095
74. Deris JB, Kim M, Zhang Z, Okano H, Hermsen R, Groisman A, et al. The innate growth bistability and fitness landscapes of antibiotic-resistant bacteria. Science. 2013;342(6162):1237435. https://doi.org/10.1126/science.1237435 PMID: 24288338
75. Frenkel N, Saar Dover R, Titon E, Shai Y, Rom-Kedar V. Bistable Bacterial Growth Dynamics in the Presence of Antimicrobial Agents. Antibiotics (Basel). 2021;10(1):87. https://doi.org/10.3390/antibiotics10010087 PMID: 33477524
76. Wright ES, Vetsigian KH. Inhibitory interactions promote frequent bistability among competing bacteria. Nat Commun. 2016;7(1):11274.
77. San Millan A, Escudero JA, Gifford DR, Mazel D, MacLean RC. Multicopy plasmids potentiate the evolution of antibiotic resistance in bacteria. Nat Ecol Evol. 2016;1(1):10. https://doi.org/10.1038/s41559-016-0010 PMID: 28812563
78. Schuster E, Taftaf R, Reduzzi C, Albert MK, Romero-Calvo I, Liu H. Better together: circulating tumor cell clustering in metastatic cancer. Trends Cancer. 2021;7(11):1020–32.
79. Yamamoto A, Doak AE, Cheung KJ. Orchestration of collective migration and metastasis by tumor cell clusters. Ann Rev Pathol Mechan Dis. 2023;18:231–56.
80. Haynes NM, Chadwick TB, Parker BS. The complexity of immune evasion mechanisms throughout the metastatic cascade. Nat Immunol. 2024;25(10):1793–808. https://doi.org/10.1038/s41590-024-01960-4 PMID: 39285252
81. Limdi A, Pérez-Escudero A, Li A, Gore J. Asymmetric migration decreases stability but increases resilience in a heterogeneous metapopulation. Nat Commun. 2018;9(1):2969. https://doi.org/10.1038/s41467-018-05424-w PMID: 30061665
82. Mishra A, Chakraborty PP, Dey S. Dispersal evolution diminishes the negative density dependence in dispersal. Evolution. 2020;74(9):2149–57. https://doi.org/10.1111/evo.14070 PMID: 32725620
83. Chakraborty PP, Nemzer LR, Kassen R. Experimental evidence that network topology can accelerate the spread of beneficial mutations. Evol Lett. 2023;7(6):447–56. https://doi.org/10.1093/evlett/qrad047 PMID: 38045727
84. Chakraborty P, Kassen R. Rapid adaptation and increased genetic parallelism in experimental metapopulations of pseudomonas aeruginosa. bioRxiv. 2024;:2024–10.
85. Chakraborty PP. The Impact of Spatial Network Topologies on the Adaptive Evolution of Pseudomonas aeruginosa Metapopulations. Université d'Ottawa| University of Ottawa; 2024.
86. Newton PK, Ma Y. Maximizing cooperation in the prisoner's dilemma evolutionary game via optimal control. Phys Rev E. 2021;103(1–1):012304. https://doi.org/10.1103/PhysRevE.103.012304 PMID: 33601552
87. Maltas J, Tadele DS, Durmaz A, McFarland CD, Hinczewski M, Scott JG. Frequency-Dependent Ecological Interactions Increase the Prevalence, and Shape the Distribution, of Preexisting Drug Resistance. PRX Life. 2024;2(2):023010. https://doi.org/10.1103/prxlife.2.023010 PMID: 40786663